Supporting Information

Spatially and time-resolved carrier dynamics in core-shell InGaN/GaN multiple-quantum wells on GaN wire

Jaime Segura-Ruiz[†], Damien Salomon[†], Andrei Rogalev[†], Joël Eymery[◊], Benito Alén[‡], and Gema Martínez-Criado[▽†],*

[†]European Synchrotron Radiation Facility, 38043-Grenoble, France

[◊]Univ. Grenoble Alpes, CEA, IRIG, MEM, NRS, 38000 Grenoble, France

[‡]Instituto de Micro y Nanotecnología, Consejo Superior de Investigaciones Científicas, 28760 Tres Cantos, Spain

[▽]Instituto de Ciencia de Materiales de Madrid, Consejo Superior de Investigaciones Científicas, 28049 Cantoblanco, Spain

S1: Details of the experimental setup and sample structure.

A pulsed hard X-ray beam from the storage ring is pre-focused horizontally by a Si mirror, and then nanofocused by mirrors [80 × 80 nm^2 spot size with 10^{12} ph/s at 29.6 keV]. The sample is raster scanned in the X-ray nanobeam, while collecting both the characteristic secondary X-rays (XRF) and light emission. Thus, XEOL and XRF spectra are recorded with a far-field optical system and an energy dispersive Si drift detector, respectively, for each raster position of the sample. The timing structure of the 16 bunch filling mode of the storage ring [5.68 MHz repetition frequency and 50 ps pulse duration] is exploited to investigate the carrier dynamics. The luminescence emitted by the sample and collected by the optical head is dispersed by a 0.3 m focal length ACTON spectrometer (grating 1200 gr/mm) and detected by a Si avalanche photodiode. Thus, the bandpass of our TRXEOL measurements is about 3 nm. Time correlated single photon counting electronics is used to record the TRXEOL decay curves. The impulse response function

(IRF) of the TRXEOL system is recorded using the visible part of the synchrotron light under the same conditions. After numerical deconvolution, the decay times are determined with a time resolution superior than 20 ps.

Thus, in our approach, besides the depth resolution, which is determined by the incident X-ray beam and its interaction with the matter (29.6 keV beam means a penetration depth of 23.6 μm in GaN at normal incidence – which is much larger than the wire thickness), the actual spatial resolution of our approach is governed by the spot size of the incident X-ray beam (80 nm) and carrier diffusion mechanisms (200−600 nm diffusion length for InGaN/GaN). Therefore, despite probing different sample depths, the elemental and optical maps collected by XRF and XEOL effectively reflect the modulation of the composition and light emission respectively by buried structures and gradients present within the whole excitation volume. Thus, our findings will reveal not only the influence of the edges and vertices of the hexagonal geometries, but also the inner variations within the GaN core.

On the other hand, the sample consists of an inner n-doped GaN core (~2 μm diameter) with five periods of InGaN/GaN MQWs shell (1.25-nm-thick InGaN well with ~15% In concentration and 10-nm-thick GaN barrier). The InGaN MWQs are deposited in both top *c*-plane and side *m*-plane facets, leading to strongly confined energy levels that provide high efficient traps for carriers. The core-shell architecture exhibits notable advantages over planar group-III nitride structures: a high tolerance to lattice mismatched substrates with a much lower density of dislocations, a large increase of the active area that limits the efficiency droop, and radial growth of nonpolar *m*-plane QWs preventing quantum confined stark effects (QCSE) that hinders the overlapping of the electron and hole wavefunctions. Polar *c*-plane GaN/InGaN MQWs exhibit electrostatic fields due to the discontinuity of the spontaneous and piezoelectric polarizations. Due to the QCSE, the energy difference between the electron and hole ground states, at which the vertical radiative transition takes place, increases quadratically with the built-in polarization-induced electrostatic field. Thus, this leads to different recombination energies depending on the crystallographic orientation of the MQWs. From the dynamic point of view, inside the quantum well, the electric field pulls the bound electron and hole in opposite directions, reducing their wavefunction overlap, and in turn decreasing their oscillator strength and hence their radiative recombination rate. For our study, the wires were detached from the substrate and then dispersed on silicon nitride membranes.

S2: Comparison: CL, PL and XEOL

It is worth to mention that the optical luminescence from CL or XEOL experiments is different from the PL induced by a laser beam. The later generates one electron hole pair from one incident photon, whereas the former can generate a few thousand electron-holes from an electron or X-ray photon. However, in comparison to a laser excitation by PL, which is almost in resonant configuration with respect to the band-gap energy of a semiconductor, by XEOL a more complex phenomenon is behind the luminescence process due to the high-energy of the incident X-rays, and subsequently the core-level photoelectrons, limiting the experiment to low injection conditions. As it is represented in Figure 1 (c), initially a core-hole is created by the annihilation of an X-ray, which is immediately filled by electrons from shallower levels mostly via Auger and XRF. Then, the new shallower core-holes left behind are filled by even shallower core or valence electrons which creates a cascade process. Thus, the energetic photoelectrons and Auger electrons create more electrons and holes in their tracks as they travel through the sample and lose energy via inelastic scattering (thermalization), until the electrons and holes thermalize at the bottom of the conduction band, and top of the valence band, respectively. Finally, these electrons and holes radiatively recombine directly and/or indirectly, producing luminescence with photon energy close to the band-gap. Furthermore, in a PL experiments we only excite carriers in a relatively small volume compared to XEOL experiments excited with a hard X-ray beam (29.6 keV), where several microns penetration depth is reached. Thus, the spatial gradient in carrier density is much larger for XEOL acquisitions, playing carrier diffusion a key dominant role. In addition, XEOL can be site specific since the core-level is specific to a given element and that it involves energy transfer via secondary processes to the optical channel (thermalization of electrons and holes). The extent of this X-ray energy conversion to optical photons depends on the excitation channel (K or L shell etc.), and the nature of the semiconductor material, e.g. crystallinity, morphology, size and proximity effects.

S3: XEOL spectra associated with each point of the axial scan displayed in Figure 5.

Figure S1 shows the XEOL spectra associated to each point of the axial scan displayed in Figure 5 of the manuscript - the centre wavelength is indicated and the bandwidth from which the time-

resolved XEOL traces have been recorded superimposed in red bars. As it has been discussed in the text, the peak energy and the spectral width change with the position. Since that the MQWs related emission bandwidths are much greater (≥ 30nm) than the instrumental bandpass (~ 3 nm indicated by red bars), then our optical system performed as if the emission "line" is a portion of a continuum. So, the bandpass could indeed be viewed as a spectral spread of ± 0.5 bandpass around the centre wavelength, making the detection of recombination times only sensitive to the dominant mechanisms contributing to the peak maximum (3 nm), and not to changes across the lineshape

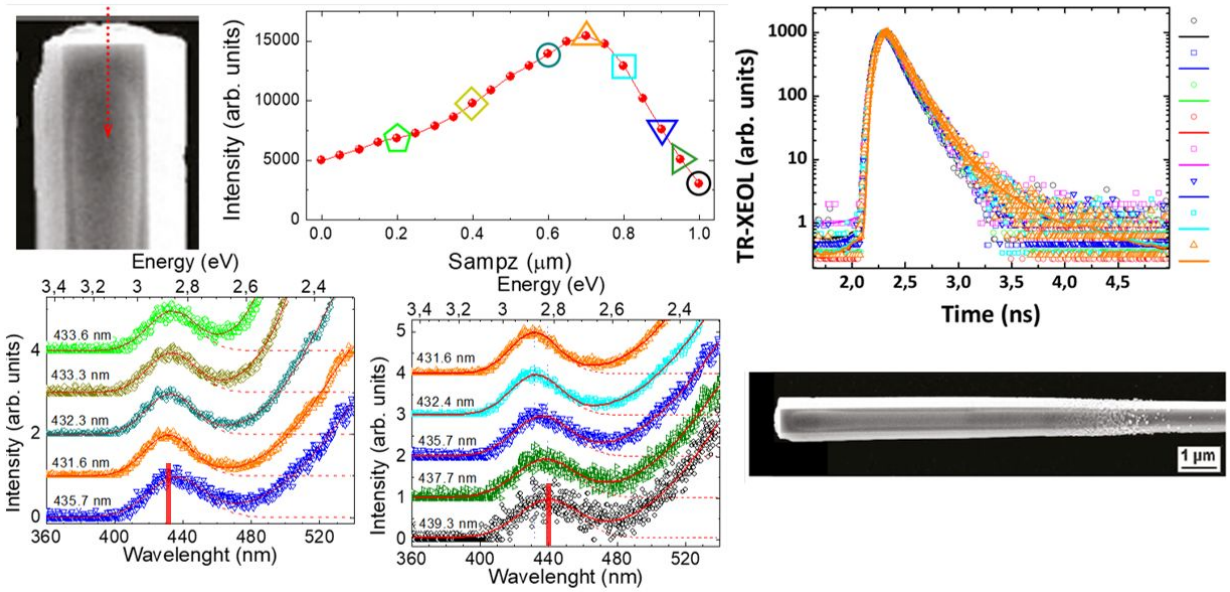

Figure S1. XEOL and TRXEOL spectra collected along the axial scan one micron length.

S4: Schematics of the band diagram for c- and m-plane GaN/InGaN QWs.

Compared to nonpolar m-plane GaN/InGaN MQWs, polar c-plane MQWs exhibit electrostatic fields due to the discontinuity of the spontaneous and piezoelectric polarizations (see Fig. S2a). Due to the Quantum Confined Stark Effect, the energy difference between the electron and hole ground states, at which the vertical radiative transition takes place, increases quadratically with the built-in polarization-induced electrostatic field. In our case, this leads to different recombination energies depending on the crystallographic orientation of the MQWs.

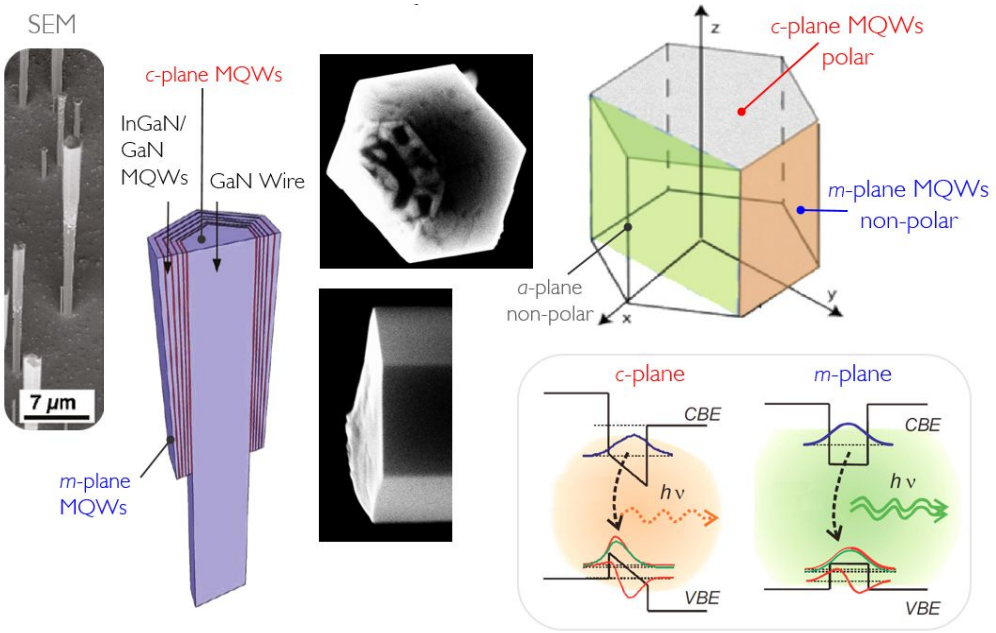

Figure S2a. SEM images of the wire morphology and schematic of the cross-sectional view of a single InGaN/GaN MQWs wire. The energy band diagrams for c- and m-plane QW is included, showing the effect of the Quantum Confinement Stark Effect.

From the dynamic point of view, inside the quantum well, the electric field pulls the bound electron and hole in opposite directions, reducing their wavefunction overlap, and in turn decreasing their oscillator strength and hence their radiative recombination rate. Hence, the strong impact of the internal electric fields plays a key role in the optical performance of advanced nano-LEDs (see Fig. S2b).

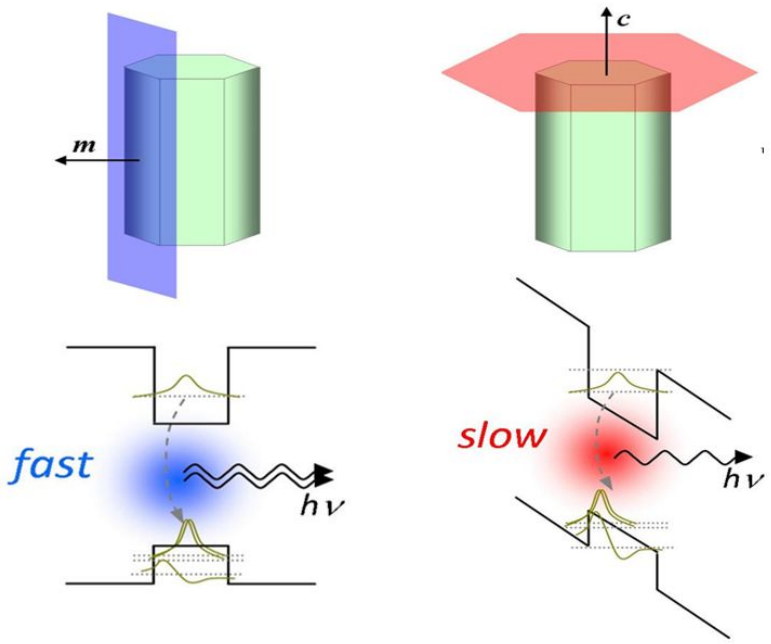

Figure S2b. Basic representation of the effect of the Quantum Confinement Stark Effect on the recombination rates for c- and m-plane QW.

S5: Detailed information on the optical spectra (peak intensity, peak wavelength and FWHM) in 2D obtained on a pixel-by-pixel basis by a multiple-Gaussian fitting procedure applied to each XEOL spectrum

Figure S3 reveals the resulting spatial distribution of the InGaN-related transition energy, line width and intensity. Our results indicate that the InGaN-related emission maxima, line shapes, and intensities are effectively correlated at the hexagon wire apex. In good agreement with our previous report, the emission intensity maxima shift to higher energy with a reduced line width highlighting the effect of the higher confinement presents at the hexagon wire apex. The black curve corresponds to an exponential decay fit performed to deduce the carrier diffusion length. The combination of spatially resolved XEOL and coaxially grown quantum structure additionally reflects the carrier diffusion in the GaN. At room temperature, we measured the XEOL spectra as a function of the X-ray beam position along the nanowire axial and radial axis with a 50 nm spacing between consecutive X-ray beam spots. Thus, the ambipolar diffusion length, Ld, can be roughly estimated by the integrated XEOL intensity of the InGaN-related emission as a function of the X ray beam position, $I_{MQW} = I_0 \exp(-x/L_d)$, where I_{MQW} is the XEOL intensity of the transition from

the InGaN MQW, x is the distance between the X-ray beam position and the MQW region, and I_0 represents a scaling factor.

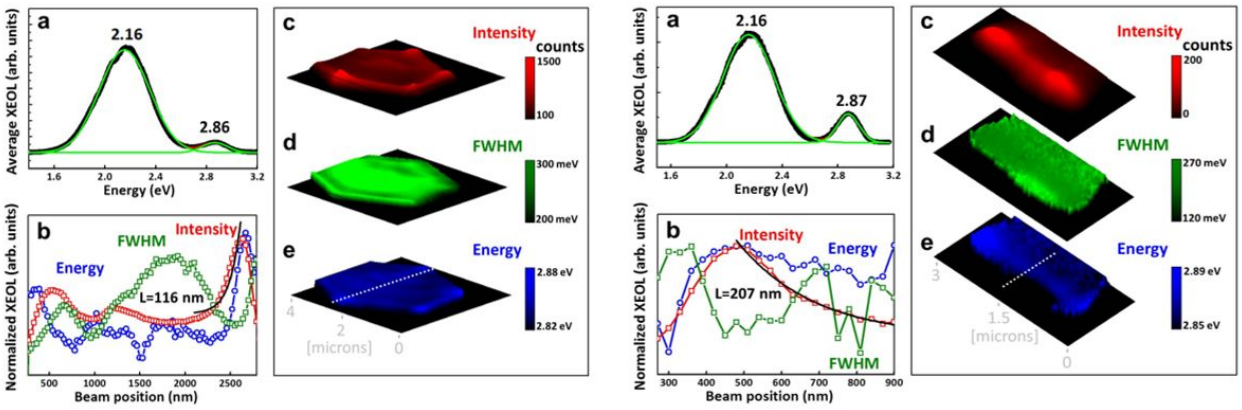

Figure S3. Spectral decomposition of the dominant transition at 2.87 eV in both excitation configurations: intensity (red), FWHM (green), and energy (blue) accompanied by the corresponding profiles taken along the white dotted line.